Bidirectional translocation of actomyosin drives epithelial invagination in ascidian siphon tube morphogenesis

Jinghan Qiao[1,#], Pengyu Yu[2,#], Hongzhe Peng[1], Wenjie Shi[1], Bo Li[2,*], and Bo Dong[1,3,*]

1 Fang Zongxi Center, MoE Key Laboratory of Marine Genetics and Breeding, College of Marine Life Sciences, Ocean University of China, Qingdao 266003, China.

2 Institute of Biomechanics and Medical Engineering, Applied Mechanics Laboratory, Department of Engineering Mechanics, Tsinghua University, Beijing 100084, China.

3 Institute of Evolution & Marine Biodiversity, Ocean University of China, Qingdao 266003, China.

# These authors contribute equally to this work

* Correspondence: bodong@ouc.edu.cn (B.D.); libome@tsinghua.edu.cn (B.L.)

Summary

How epithelia preform a spatiotemporal heterogeneous force generating program to drive a sequential tissue morphogenesis remains unclear, particularly the underlying precise mechanical mechanisms. This study investigated dynamic actomyosin reorganization between apical and lateral membrane cortex regions during two sequentially invaginated stages during ascidian atrial siphon tube morphogenesis. At the initial invagination stage, the originally lateral-located actomyosin translocated to the apical domains, while those actomyosin re-translocated back to lateral domains at the accelerated invagination stage. Using genetic mutants to modulate myosin activities, the initial invagination was strengthened or abolished, indicating invagination are apical constriction dependent. Optogenetic inhibition of myosin activities in lateral domains after initial invagination stage blocked the further processes, suggesting lateral constriction of actomyosin is required for the accelerated invagination. Vertex model simulations uncovered a coupled mechanism underlying epithelial invagination driven by apicobasal tension imbalance and lateral contraction. We thus propose an actomyosin translocation mechanical model: lateral actomyosin first translocate apically to drive apical constriction and shape the initial invagination, then apical actomyosin redistributes laterally to promote lateral contractility and accelerate invagination. Our findings discovery a bidirectional reorganization of actomyosin network as a central mechanism driving epithelial invagination, providing insights on epithelial invagination and the organ morphogenesis during development.

Keywords

Ciona; atrial siphon; epithelial invagination; translocation; vertex model

Introduction

Morphogenesis, by which cells and tissues acquire their shape and structure, is a central theme in developmental biology. The tissue shape transformation in morphogenesis is fundamentally driven by the spatiotemporally regulated biomechanical forces(Collinet & Lecuit, 2021; Matter & Balda, 2003; Štorgel et al., 2016). The generation and conduction of biomechanical forces play as an essential mechanism of morphogenesis, via regulating cell rearrangement, division, and deformation at both cellular and tissue scales(Chan et al., 2017; Lecuit et al., 2011; Matter & Balda, 2003; Nagafuchi, 2001; Osswald et al., 2022; Tepass, 2002). Among these, actomyosin contractility plays a pivotal structure generating biomechanical tension in subcellular level, which is the basic of cell and tissue-level morphogenesis(Chung et al., 2017; Even-Ram et al., 2007; Fristrom, 1988; Lee & Harland, 2007; Popkova et al., 2024; Vicente-Manzanares et al., 2009; Zartman & Shvartsman, 2010). Despite the widely acknowledged critical role of bio-mechanical forces in morphogenesis, the precise mechanisms by which these forces regulate cell and tissue remodeling, particularly how cells reorganize contractile domains in space and time to coordinate sequential morphogenetic events remains a significant challenge.

A typical example of morphogenesis is the transition from simple epithelial sheets to complex three-dimensional architectures(Collinet & Lecuit, 2021). A large number of previous researches demonstrated the function of apical constriction in epithelial sheet invagination, such as in the invagination process of the *Drosophila* embryonic trachea(Schottenfeld et al., 2010) and salivary gland placode(Pearl et al., 2017). However, more and more studies noticed that the apical constriction itself is not sufficient in shaping complex epithelial three-dimensional structures and various epithelial tube shapes(Kondo & Hayashi, 2013; Pearl et al., 2017). So, an interesting question is how do epithelial cells preform a spatiotemporal heterogeneous force generating program to drive a sequential epithelial tissue reshaping.

Marine ascidian *Ciona* is an excellent model for studying morphogenesis due to its simple developmental process, transparent embryos, and its close evolutionary relationship with vertebrates(Blair & Hedges, 2005; Delsuc et al.,

2006; Zhao et al., 2021). For example, asymmetrical actomyosin contractility in notochord was demonstrated to provide force for tail bending(Lu et al., 2020; Peng et al., 2020). Actomyosin sequentially localized on the apical and basolateral cell surfaces to drive the endodermal invagination(Fiuza & Lemaire, 2021; Hotta et al., 2007; Kourakis et al., 2010). Local myosin activation coupled with junctional rearrangements drives directional zippering(Hashimoto & Munro, 2019; Hashimoto et al., 2015) in neural tube closure, and cell cortex distribution and the stability of tight junctions (TJs) were essential for notochord tube lumen opening and expansion(Shi et al., 2025).

Ciona and vertebrates share evolutionary developmental homology. There may be a potential homology between the otic placode of vertebrates and the atrial siphon primordium of *Ciona*(Kourakis et al., 2010). The atrial siphon forms from a non-dividing region in the lateral-dorsal epidermis of the head and follows a separate developmental trajectory(Hotta et al., 2020; Kourakis et al., 2010). Invagination initially generates shallow pits, which later deepen and connect to the gut lumen after metamorphosis, creating two atrial siphons(Hotta et al., 2007; Kourakis et al., 2010). Eventually, the left and right siphons fuse to form a single atrial siphon(Chiba et al., 2004). Despite these observations, the early cellular events during atrial siphon tube morphogenesis remain incompletely understood.

In this study, we investigated the morphogenesis of the *Ciona* atrial siphon. Firstly, the detailed cellular process of *Ciona* atrial siphon formation through initial and the accelerated stages was described by visualizing cell boundary and nuclei. By combining actomyosin localization analysis, genetic manipulation, and vertex model simulations, we demonstrated that lateral actomyosin first translocated apically to drive apical constriction and established the initial invagination, then redistributed laterally to promote cell shortening and the further atrial siphon tube invagination. Disruption of myosin activity altered invagination timing, while optogenetic inhibition of myosin activity after initial apical constriction stage blocked the further invagination. Furthermore, a cell-based vertex model was established to validate the relationship between contractile force redistribution and epithelial invagination. The coupled biomechanical mechanisms induced by apicobasal imbalance and lateral contraction were uncovered as fundamental determinants of the

atrial siphon invagination. These results provide new insights into the biomechanical control of tissue morphogenesis, and highlight the value of marine model organisms for addressing fundamental questions in developmental biology.

Results

The cellular processes of *Ciona* atrial siphon invagination

To investigate the early cellular events during atrial siphon morphogenesis, we performed actin filament (F-actin) staining on the fixed samples to capture the detailed cellular dynamics (Figure 1A). The cell at the bottom center of the invaginating region was defined as the “center cell” (Figure 1B). Measurements taken at different stages included the height and apical-to-basal area ratio of the center cell, the invagination depth of the atrial siphon and the linear distance between the -3/-4 and +3/+4 cell junctions (Figure 1B-E, Figure 1—figure supplement 1). At the initial invagination stage (13.5-16.0 hpf), the center cell height increased, the apical-to-basal area ratio decreased, and the protruding cell surface became inward pit, but no significant invagination occurred (Figure 1A), as reflected by a low invagination slope (k = 0.2617). During the accelerated stage (16.0-18.0 hpf), the center cell height decreased, the apical-to-basal area ratio stabilized, and invagination progressed rapidly (k = 2.7920). EdU incorporation and TUNEL assays demonstrated that neither cell division nor apoptosis was involved in the whole invagination process (Figure 1—figure supplement 2).

Bidirectional translocation of actomyosin between apical and lateral domains during atrial siphon tube invagination

To analyze the forces driving atrial siphon tube invagination, we first visualized the distribution of F-actin and quantified its dynamics at different cellular domains (Figure 1—figure supplement 1A). During the initial invagination stage, before 15 hpf, F-actin concentration decreased at the lateral domains, while gradually increased around the apical membrane, resulting in a higher F-actin accumulation at the apical region. Subsequently, the F-actin concentration at lateral region started to increase and exceeded that in the

apical domain after 16 hpf, during which apical F-actin levels showed a gradual decline (Figure 1—figure supplement 1A).

Using anti-pS19 MRLC antibody, we examined the spatial and temporal patterns of myosin activity within the atrial siphon primordium. Quantification of signal intensities from the apical, basal, and lateral regions during the initial and the accelerated stages showed that the distribution pattern of active myosin was consistent with that of F-actin (Figure 2A, B). Specifically, active myosin and F-actin levels were higher at the apical region than the lateral one during the initial stage, whereas the opposite pattern was observed during the accelerated stage (Figure 2B).

Additionally, top view imaging showed that during the initial stage, atrial siphon primordium cells were arranged in a circular pattern (Figure 2A). Active myosin exhibited a similar ring-like localization, suggesting that the early stages of atrial siphon morphogenesis are driven by circumferential contractile forces generated by phosphorylated myosin, facilitating inward constriction of the primordium (Figure 2A, B). Furthermore, quantification of the lateral cell distance (Figure 1—figure supplement 1B) demonstrated a reduction in spacing between peripheral cells, indicating that surrounding cells moved centripetally toward the center position.

Integrating the localization of actomyosin with the observed cell shape changes, we propose a hypothesis in which the bidirectional reorganization of contractile forces at the apical and lateral regions drives epithelial invagination during atrial siphon morphogenesis (Figure 2C). Initially, actomyosin translocated from the lateral regions to the apical domains, generating contractile forces for apical constriction (Figure 1—figure supplement 1A). Meanwhile, the inward compression from surrounding cells facilitates cell elongation, establishing the initial invaginated cell morphology and preparing for subsequent morphogenesis (Figure 1—figure supplement 1B). Then, actomyosin translocated from the apical domains to the lateral regions, generating contractile forces that promoted center cell shortening and accelerate the tissue invagination (Figure 2C).

Center cell height is coupled with invagination depth

To further verify our hypothesis and explore the relationship between myosin

contractility, force redistribution, and the progression of invagination, we overexpressed MRLC (T18ES19E)::mCherry (a diphosphorylated mutant that enhances myosin activity)(Espinoza-Fonseca et al., 2014), MRLC (T18AS19A)::mCherry (an unphosphorylated mutant that reduces myosin activity)(Iwasaki et al., 2001) and MRLC::mCherry (wild-type control) in the atrial siphon primordium to modulate contractile force in embryos, respectively (Figure 3A, B). The results showed that the invagination initiated earlier (15 hpf) compared to control group in MRLC (T18ES19E)-expressed embryos. At 16 hpf, MRLC (T18ES19E) group exhibited a deeper invagination and shorter center cell height. In contrast, in MRLC (T18AS19A) group, the invagination initiation time was delayed. Even at 16 hpf, the center cell height did not decrease and the invagination did not occur (Figure 3B). Notably, the increase in invagination depth is strongly correlated with the reduction in center cell height, with both changes occurring synchronously across experimental groups with different myosin activities (Figure 3B). These results demonstrate a strong coupling between the reduction in center cell height and the increase in invagination depth, suggesting that this process is closely associated with the redistribution of myosin localization from the apical to lateral regions as invagination progresses.

Inhibition of myosin activity during apical-to-lateral redistribution impedes invagination progression

To further examine the necessity of the redistribution of myosin between the apical and lateral regions during invagination, we utilized an optogenetic MLCP-BcLOV4(Berlew et al., 2021; Berlew et al., 2020; Berlew et al., 2022; Glantz et al., 2019; Glantz et al., 2018; Yamamoto et al., 2021) system (Figure 4A) to specifically inhibit myosin II activity at the critical redistribution time point between the initial invagination and the accelerated invagination stage (16-17 hpf). This system has been proven to effectively reduce the contractility of epidermal cells in *Ciona* embryos(Qiao et al., 2023). Compared to the control group (Figure 4—figure supplement 1) and dark treatment group, the experimental group with 1 h light exposure, which activated the optogenetic system, blocked further invagination (Figure 4B, Figure 4—video 1, 2), and while invagination ceased to deepen, the center cell height did not show a

significant decrease (Figure 4C, D). These results confirm that the redistribution of myosin contractility from the apical to lateral regions is essential for the development of invagination.

Vertex model simulations recapitulate the mechanical process of ascidian siphon tube invagination

To validate the hypothesis that the redistribution of contractile forces drives invagination, we developed a cell-based vertex model(Alt et al., 2017) and performed simulations for atrial siphon morphogenesis. The cross-section of the epithelial cells is represented by two-dimensional polygons with vertices and edges. The interaction between the epithelia and the other cells below, which function as structural support, are simplified as a basal elastic force (Figure 5A). Cell deformation and tissue morphology are simulated by the motion of vertices, which is controlled by the constraint of cell area and cortical contraction, tissue surface bending, and most importantly, active line tension dynamics (Figure 5A, see Methods). The active tension $\Gamma_J^{\mathrm{a,b,l}}$, on the apical, lateral and basal edges of a specific cell J, are induced by dynamic production and distribution of actomyosin $m_J^{\mathrm{a,b,l}}$ on corresponding regions through a tension coefficient k_{m} (Figure 5B). Here we use the apical and lateral F-actin fluorescence intensities normalized by inactive basal intensity measured in experiments (Figure 1—figure supplement 1A) to describe the evolution of actomyosin intensity in the center cell of the model. The actomyosin intensity in adjacent 9 cells (-4 to +4) are linearized from inactive to active $m_{\mathrm{exp}}^{\mathrm{a,l}}$ (see Methods). We applied the periodic boundary conditions along x axis to avoid the boundary effect, and reduced the periodic length in simulations to mimic the decreased distance between adjacent cells obtained from experiments (Figure 1—figure supplement 1B). The numerical simulations were conducted based on an initial flat epithelial shape consisting of $N = 25$ cells at 13 hpf to examine the morphological processes driven by active tensions (see Methods).

Our mechanical model successfully reproduced the invagination of the atrial siphon observed in experiments (Figure 5C, D, Figure 5—Video 1). During the initial stage, the rapid accumulation of actomyosin on the apical

surface gave rise to apical tension. The active tension induced the contraction of central region and led the adjacent cells to migrate to the center cells, which induced the cell elongation and apicobasal imbalance, breaking the apicobasal symmetry and initializing the invagination into the basal side. After 15 hpf, the lateral actomyosin intensity increased significantly and induced high tension on the lateral surface, pulling cells and shortening the cell height. The coupling apico-lateral contraction further facilitated the invagination, which gave rise to the siphon-like epithelial shape formation at 18 hpf (Figure 5D). The invagination depth and center cell height were quantified during this process and were consistent with the experimentally measured data (Figure 5C). We further varied both apical and lateral actomyosin intensities m by introducing a scaling factor α to experimental measured $m_{\exp}$ as $m = \alpha m_{\exp}$ into the model, to simulate unphosphorylated or diphosphorylated mutants whose overall myosin activities in cells are altered in experiments (Figure 3). As anticipated, simultaneous enhancement of apical and lateral actomyosin activities significantly increased invagination depth while reducing center cell height (and vice versa), closely corresponding with experimental mutant data (Figure 5E, F). These results validate the validity of our model in capturing the mechanical process of ascidian siphon tube invagination.

Coupled mechanism of apicobasal bending and lateral contraction via actomyosin redistribution

To theoretically distinguish the effects of apical and lateral contraction on morphogenesis, we performed perturbation on the intensity of regional actomyosin. The apical actomyosin intensity m^{a} was modulated as $m^{\mathrm{a}} = \alpha_{\mathrm{a}} m^{\mathrm{a}}_{\exp}$, where $m^{\mathrm{a}}_{\exp}$ represented the experimental data shown in Figure 5B. As a result, the invagination depth increased significantly under higher α_{a} (Figure 6A), while the central height remained relatively independent of α_{a} when $\alpha_{\mathrm{a}} \geq 0.6$ (Figure 6B). Intriguingly, the depth value became negative when $\alpha_{\mathrm{a}} \leq 0.2$, which meant the invagination cannot occur but was replaced by evagination, where the decrease of the central height after 15 hpf also disappeared. This inversion of the tissue shape was attributed to the inversion of apico-basal

differential of actomyosin intensity (Figure 6C), in which a low α_a resulted in apical actomyosin intensity falling below the reference basal intensity. These results suggest a bending mode under an equivalent moment induced by apico-basal tension imbalance, which breaks tissue symmetry and determines the buckling direction, facilitating the invagination without obviously affecting the cell height. In contrast, under modified lateral actomyosin, the central height varied distinctly (Figure 6D) with mild invagination depth variation (Figure 5B). This indicated that lateral tension primarily facilitates tissue invagination by regulating cellular contraction along the thickness direction, representing a lateral contraction mode. Collectively, these results demonstrate that the invagination of the atrial siphon is mediated by the coupled biomechanical mechanism of a bending mode induced by apicobasal tension imbalance and a contraction mode driven by lateral tension.

Finally, to clarify the characteristics of actomyosin redistribution between apical and lateral regions, we calculated the total actomyosin intensity $S_c = m_c^{\mathrm{a}} + m_c^{\mathrm{l}}$ and the ratio of apical and lateral intensity $R_c = m_c^{\mathrm{a}} / m_c^{\mathrm{l}}$ in the center cell (Figure 6E). During the whole morphogenesis, S_c increased persistently, providing the driving force underling epithelial invagination. While a significant peak value in the curve of R_c was observed during the initial stage, representing the translocation from lateral to apical regions during 14-15 hpf and a reverse translocation during 15-16 hpf (Figure 6E). To investigate the translocation effect quantitively, we modified the translocation level after 14 hpf in the model as $R_c = \beta(R_{\exp} - 1) + 1$, where β is the translocation intensity controlling the redistribution ratio. As shown in Figure 6F, varying total actomyosin $S_c = \alpha S_{\exp}$ and apical-lateral translocation R_c controlled by α and β, respectively, were introduced into simulations. Computational results indicated that the overall invagination magnitude (Figure 6G) is predominantly regulated by the total actomyosin intensity within cells, whereas stronger regional translocation and redistribution contribute to the rapid reduction in height of invaginating cells (Figure 6H), thereby ensuring direct cell shape changes that support robust atrial siphon formation in the ascidian.

Discussion

The morphogenesis of the *Ciona* atrial siphon provides a compelling model to dissect how biomechanical forces orchestrate tissue invagination. Our study revealed that actomyosin contractility underwent a dynamic spatial redistribution during this process, initially translocating from the lateral cortex to the apical region to promote apical constriction and establish the initial cell shape, and subsequently redistributing back to the lateral regions to promote center cell shortening and accelerate the tissue invagination. By combining actomyosin localization analysis, genetic perturbations, optogenetic manipulation, and vertex model, we established a mechanistic framework linking force dynamics to tissue remodeling. This work not only advances our understanding of siphon morphogenesis but also offers broader insights into the principles governing force-driven tissue shaping in developing organisms.

Our findings demonstrated that the atrial siphon invagination was driven by a coupled mechanism including apicobasal tension imbalance and lateral contraction in a two-stage process. During the initial stage (13.5-16.0 hpf), actomyosin translocated from the lateral cortex to the apical cortex, generated contractile forces that induced apicobasal tension imbalance and reduced apical cell area and elongated the primordium. This aligns with classical models of epithelial folding, where apical actomyosin networks drive tissue curvature through localized contraction, often accompanied by an increase in cell height, as observed in the invagination of the *Drosophila* embryonic trachea(Schottenfeld et al., 2010) and salivary gland placode(Pearl et al., 2017). Additionally, in traditional invagination models, various epithelial tissues use different mechanisms to drive deeper invagination. In *Drosophila* tracheal development, for instance, mitosis acts as a critical turning point in accelerating invagination(Kondo & Hayashi, 2013). During the early slow phase of tracheal invagination, apical constriction under EGFR signaling, forms a shallow pit. As invagination transitions into a rapid phase, mitotic entry induces cell rounding, which increases tension and epithelial buckling, thereby accelerating the invagination process and facilitating the internalization of placode cells(Kondo & Hayashi, 2013; Nishimura et al., 2007). Moreover, cell apoptosis can also expedite the invagination process, as seen in *Drosophila*

leg morphogenesis, where actomyosin cables formed in apoptotic cells help trigger the invagination(Kiehart, 2015; Manjón et al., 2007; Monier et al., 2015). Distinct from these classical models, the accelerated invagination stage of *Ciona* atrial siphon morphogenesis was driven by a critical redistribution of apical actomyosin to the lateral regions, during accelerated stage (16.0–18.0 hpf), providing a force-generating mechanism for invagination progression without relying on cell proliferation or apoptosis to accelerate the process. The lateral enrichment of p-MLC correlated with a reduction in center cell height and the initiation of invagination, suggesting that lateral forces actively pulled the tissue inward. This spatial redistribution of contractile forces in *Ciona* atrial siphon invagination is reminiscent of mechanisms observed in certain epithelial folding processes, such as the *Drosophila* wing disc, where invagination is not solely driven by apical constriction but can also result from increased lateral tension or reduced basal tension(Sui et al., 2018). Our optogenetic inhibition of myosin activity during the apical-to-lateral redistribution—using the MLCP-BcLOV4 system—directly confirmed that this redistribution was not merely a passive consequence of invagination but was an active driver of the process.

Our study revealed a strong coupling between cellular shape changes and tissue remodeling during *Ciona* atrial siphon invagination, where the reduction in center cell height was closely associated with invagination depth. Tissue morphogenesis emerges from the integrated actions of multiple cellular behaviors, such as contraction, adhesion, and migration, that work in concert to remodel epithelial architecture(Chan et al., 2017). The transmission of local cell-generated forces across tissues is further shaped by mechanical cues and geometric constraints, enabling the transformation of cellular-scale changes into organ-scale morphogenesis(Collinet & Lecuit, 2021). By perturbing myosin activity, we found that this coupling was directly regulated: dominant-negative myosin mutants delayed both processes, whereas hyperactive myosin accelerated invagination. The quantitative agreement between vertex model analysis and experimental measurements validated the critical role of actomyosin contractility dynamics in linking cellular shape changes to tissue remodeling. Furthermore, the model also uncoupled the effects of the actomyosin in different domains, and predicted that stronger

apical-lateral translocation facilitates the rapid reduction in height of invaginating cell. The *Ciona* atrial siphon, which underwent invagination without cell proliferation or apoptosis, provided a minimal system for investigating the role of biomechanical forces in tissue remodeling. Our findings emphasized that the deformation of a few key cells under spatially precise mechanical regulation, along with their coordination with surrounding tissues, is crucial for proper morphogenesis.

While this study clarified the role of actomyosin redistribution in atrial siphon invagination, several open questions remain regarding the molecular mechanisms underlying this process. One key question is what molecular signals drive the apical-to-lateral redistribution of contractility. Possible candidates include Rho GTPase pathways(Martin et al., 2016), which regulate myosin activation; apical-basal polarity(Peng et al., 2020), which coordinate actin reorganization during morphogenesis; and mechanosensitive ion channels that respond to tissue strain(Jin et al., 2020). Additionally, the role of cell-cell adhesion and extracellular matrix remodeling in mediating force transmission during invagination requires further investigation. Using tension sensors or perturbing adhesion molecules may provide new insights into these interactions. Although our vertex model effectively predicts the contribution of force redistribution to invagination, the spatiotemporal evolution of actomyosin could also be affected by mechanosensitive pathways while generating active contraction in morphogenesis, which constructs a bidirectional loop of actomyosin regulation. Future theoretical developments should focus on integrating mechanochemical feedback linking molecular signaling with tissue-level deformation to explain robust morphogenesis.

Materials and Methods

Experimental animals' preparation and electroporation

Ciona adults were collected from the coast of Qingdao and Rongcheng, Shandong, China. They were maintained in the laboratory seawater circulation system under constant light conditions to maintain their stability. Mature eggs and sperm were separately collected from the dissected adults and subsequently mixed for fertilization. The Fertilized eggs were dechorionated in

seawater containing 1 % sodium thioglycolate (T0632; Sigma), 0.05 % protease E (P5147; Sigma) and 0.032 M NaOH. The dechorionated eggs were then used for plasmid electroporation based on the previous technique procedure(Christiaen et al., 2009). Finally, the embryos were cultured in an agar-coated dish with microporous-filtered seawater in 18℃ for further observation. Detailed key resource information is annotated in Appendix 1—table 1.

Plasmid construction

Ciona myosin II light chain (MRLC) was amplified with primers MRLC-F and MRLC-R (Table S1). MRLC-mCherry(Dong et al., 2011); MRLC(T18AS19A)-mCherry and MRLC(T18ES19E)-mCherry(Denker et al., 2015); MLCP-BcLOV4 and MLCP(Qiao et al., 2023) were amplified with the primers listed in Appendix 1—table 2.

Immunofluorescence

Ciona embryos were fixed with stationary liquid(Sherrard et al., 2010), which consisted of 100 mM HEPES (pH 6.9); 100 mM EGTA (pH 7.0); 10 mM MgSO4; 2% formaldehyde; 0.1% glutaraldehyde; 300 mM dextrose and 0.2% Triton X-100 for 40 m at room temperature. Following fixation, the embryos were washed three times with PBS and subsequently incubated in PBST (PBS supplemented with 0.1% Triton X-100) for 30 m to enhance permeability. To reduce autofluorescence, embryos were treated with 0.1% sodium borohydride in PBS for 20 m at room temperature. For immunostaining, embryos were incubated with a 1:250 dilution of Phospho-Myosin Light Chain 2 (Ser19) antibody (#3671: Cell Signaling) at room temperature for 24 h. After three additional washes with PBS, a 1:200 dilution of Alexa Fluor 568 anti-Rabbit IgG (A11011: Invitrogen) was added and incubated at room temperature for 48 h. For cell boundary visualization, embryos were stained with Alexa Fluor 488 Phalloidin (A12379: Invitrogen) at a 1:200 dilution. Finally, after three washes with PBS, embryos were mounted in DAPI-containing mounting medium and prepared for imaging.

Imaging and optogenetics

Live imaging, photoactivation experiments, and image acquisition were performed using a Zeiss LSM 980 confocal microscope (Carl Zeiss). For optogenetic experiments, *Ciona* embryos were placed in a 35 mm glass-bottom dish for imaging. To activate the optogenetic system, the designated region of interest was exposed to a 488 nm laser for 1 h. The control group for dark treatment was placed in a dark box at the same temperature for 1 h. All images were analyzed and quantified using ImageJ (version 1.54p, NIH) and Imaris (version 9.0.1, Bitplane).

Vertex model simulations

***Model description*.** The epithelial cells are represented by two-dimensional polygons with vertices and edges. Vertices on the apical surface of cells are subject to no boundary constraints, while vertices on the basal surface interact with basal spring forces to simulate the structural support provided by subjacent cells (Figure 5A). The potential energy of the tissue is formulated by

$$\begin{aligned} U = &\sum_J \frac{1}{2} K_{\mathrm{A}} \left(A_J - A_0 \right)^2 + \sum_J \frac{1}{2} K_{\mathrm{C}} L_J^2 + \sum_{i_{\mathrm{a,b}}} \frac{1}{2} K_{\mathrm{B}} (\cos\theta_i - 1)^2 \\ &+ \sum_J (\Gamma_J^{\mathrm{a}} l_J^{\mathrm{a}} + \Gamma_J^{\mathrm{b}} l_J^{\mathrm{b}} + \frac{1}{2} \Gamma_J^{\mathrm{l}} l_J^{\mathrm{l}}) + \sum_{i_{\mathrm{b}}} k_{\mathrm{bm}} (r_{yi} + \frac{h_0}{2})^2, \end{aligned} \tag{1}$$

where the six terms result from, respectively, cell area control, cell cortex contractility, surface bending energy, active line tensions on apical, basal, and lateral surfaces, and subjacent interactions. K_{A} is the cell area modulus, and A_J and A_0 are the current and preferred areas of the Jth cell, respectively. K_{C} denotes the passive cortical contraction coefficient of cells and L_J represents the cell perimeter. K_{B} denotes the bending modulus of the monolayer and θ_i is the angle between the neighboring apical or basal edges of vertex i. Γ_J^{a}, Γ_J^{b}, and Γ_J^{l} are the active line tensions acting on the apical, basal, and lateral surfaces of the Jth cell with edge lengths l_J^{a}, l_J^{b} and l_J^{l}, respectively. k_{bm} is the elastic coefficient of basal interaction and h_0 is the initial cell height. $\mathbf{r}_i = (r_{xi}, r_{yi})$ denotes the Cartesian coordinates of vertex i. $\sum_J$ stands for the summation over all cells and $\sum_{i_{\mathrm{a,b}}}$ runs over all apical and basal vertices.

To describe the cell actomyosin evolution during the morphogenesis, the line tensions Γ_J^{a}, Γ_J^{b}, and Γ_J^{l} are proportional to actomyosin levels on the apical, basal, and lateral surfaces of the cell J as

$$\Gamma_J^{\mathrm{a}} = k_{\mathrm{m}} m_J^{\mathrm{a}},\ \Gamma_J^{\mathrm{b}} = k_{\mathrm{m}} m_J^{\mathrm{b}},\ \Gamma_J^{\mathrm{l}} = k_{\mathrm{m}} m_J^{\mathrm{l}}, \tag{2}$$

where k_{m} is the tension coefficient based on the myosin intensity m_J^{a}, m_J^{b} and m_J^{l}. Given that the intensity of F-actin in the center cell has been measured as $m_{\mathrm{exp}}^{\mathrm{a,b,l}}$ during the development, we define $m_{\mathrm{exp}}^{\mathrm{a,b,l}}$ as the actomyosin intensity of the center cell in the model (Figure 5B).

Simulation scheme. In the simulations, we set the cell number $N = 25$ and a periodic boundary condition in the x direction with periodic box length $L = NA_0 / h_0$. The central nine cells (index -4 to +4) are considered as active cells under contractile forces whose actomyosin intensity varies in different stages. The other cells are observed to be inactive whose actomyosin intensities are always equal to $m_0 = m_{\mathrm{exp}}^{\mathrm{b}} = 1$. The actomyosin intensities of the central nine cells (-4 to +4) are calculated through linear interpolation between inactive m_0 of boundary cells and active $m_{\mathrm{exp}}^{\mathrm{a,l}}$ of the most center cell according to the distance. The periodic length L in simulations is reduced slowly to mimic the decreased distance between adjacent cells obtained from experiments (Figure 1—figure supplement 1B). In our simulations, tissue morphogenesis is represented by vertices motion and cell deformation. The motion of vertex i obeys the Langevin equation

$$\eta \frac{\mathrm{d}\mathbf{r}_i}{\mathrm{d}t} = -\frac{\partial U}{\partial \mathbf{r}_i}, \tag{3}$$

where η denotes the damping coefficient. The equation was numerically solved using the forward Euler method with a time step of 0.01, using MATLAB R2021a. Simulations are run until $t = 400$, which corresponds to 18 hpf in experimental development with the time scale $\tau = 45\ \mathrm{s}$. The length scale $\varepsilon = 8.91\ \mu\mathrm{m}$ is determined by the normalization of initial height h_0 in model under real center cell height. The other parameters are all normalized with the time scale $\tau = 45\ \mathrm{s}$, length scale $\varepsilon = 8.91\ \mu\mathrm{m}$, and damping coefficient η. Dimensionless parameters are set as follows: $K_{\mathrm{A}} = 1$, $K_{\mathrm{C}} = 0.01$, $K_{\mathrm{B}} = 0.03$,

$k_{bm} = 0.1$, $k_m = 0.002$, $A_0 = 1$, and $h_0 = 1.25$. These parameter values are determined by numerical simulations under which the simulated invagination depth and center cell height imitates the experimental observations.

Acknowledgements

We are grateful to all members of the Fang Zongxi center for helpful discussions.

Competing interests

The authors declare that they have no known competing financial interests or personal relationships that could have appeared to influence the work reported in this paper.

Author contributions

B.D., B.L. J.Q., P.Y. conceived of the study; B.D., J.Q., P.Y., B.L., H.P., and W.S. analyzed data; P.Y. and B.L. designed the vertex model; B.D., J.Q., P.Y. and B.L. wrote the original draft. All authors approved the final version of the article.

Funding

This work was supported by the Science & Technology Innovation Project of Laoshan Laboratory (Nos. LSKJ202203204), the National Key Research and Development Program of China (2022YFC2601302), and the Taishan Scholar Program of Shandong Province, China (B.D.).

Data and resource availability

Lead contact

Requests for further resources should be directed to, and will be fulfilled by, the lead contact, Bo Dong (bodong@ouc.edu.cn).

Materials availability

All unique/stable reagents generated in this study are available from the lead contact with a completed materials transfer agreement.

Data and code availability

Model code and data are available upon request, and any additional information required to reanalyze the data reported in this paper is available from the lead contact upon request.

References

Alt S, Ganguly P, Salbreux G (2017). **Vertex models: from cell mechanics to tissue morphogenesis** *Philosophical Transactions of the Royal Society of London. Series B, Biological Sciences* **372**:20150520. https://doi.org/10.1098/rstb.2015.0520

Berlew E E, Kuznetsov I A, Yamada K, Bugaj L J, Boerckel J D, Chow B Y (2021). **Single-component optogenetic tools for inducible RhoA GTPase signaling** *Advanced Biology* **5**:e2100810. https://doi.org/10.1002/adbi.202100810

Berlew E E, Kuznetsov I A, Yamada K, Bugaj L J, Chow B Y (2020). **Optogenetic Rac1 engineered from membrane lipid-binding RGS-LOV for inducible lamellipodia formation** *Photochemical and Photobiological Sciences* **19**:353-361. https://doi.org/10.1039/c9pp00434c

Berlew E E, Yamada K, Kuznetsov I A, Rand E A, Ochs C C, Jaber Z, Gardner K H, Chow B Y (2022). **Designing single-component optogenetic membrane recruitment systems: The Rho-Family GTPase signaling toolbox** *ACS Synthetic Biology* **11**:515-521. https://doi.org/10.1021/acssynbio.1c00604

Blair J E, Hedges S B (2005). **Molecular phylogeny and divergence times of deuterostome**

561 **animals** *Molecular Biology and Eevolution* **22**:2275-2284.
562 https://doi.org/10.1093/molbev/msi225
563
564 Chan C J, Heisenberg C P, Hiiragi T (2017). **Coordination of morphogenesis and cell-fate**
565 **specification in development** *Current Biology* **27**:R1024-r1035.
566 https://doi.org/10.1016/j.cub.2017.07.010
567
568 Chiba S, Sasaki A, Nakayama A, Takamura K, Satoh N (2004). **Development of *Ciona***
569 ***intestinalis* juveniles (through 2nd ascidian stage)** *Zoological Science* **21**:285-298.
570 https://doi.org/10.2108/zsj.21.285
571
572 Christiaen L, Wagner E, Shi W, Levine M (2009). **Electroporation of transgenic DNAs in the**
573 **sea squirt *Ciona*** *Cold Spring Harbor Protocols* **2009**:pdb.prot5345.
574 https://doi.org/10.1101/pdb.prot5345
575
576 Chung S, Kim S, Andrew D J (2017). **Uncoupling apical constriction from tissue invagination**
577 *eLife* **6**:e22235. https://doi.org/10.7554/eLife.22235
578
579 Collinet C, Lecuit T (2021). **Programmed and self-organized flow of information during**
580 **morphogenesis** *Nature Reviews Molecular Cell Biology* **22**:245-265.
581 https://doi.org/10.1038/s41580-020-00318-6
582

583 Delsuc F, Brinkmann H, Chourrout D, Philippe H (2006). **Tunicates and not cephalochordates**
584 **are the closest living relatives of vertebrates** *Nature* **439**:965-968.
585 https://doi.org/10.1038/nature04336
586
587 Denker E, Sehring I M, Dong B, Audisso J, Mathiesen B, Jiang D (2015). **Regulation by a**
588 **TGFβ-ROCK-actomyosin axis secures a non-linear lumen expansion that is essential**
589 **for tubulogenesis** *Development* **142**:1639-1650. https://doi.org/10.1242/dev.117150
590
591
592 Dong B, Deng W, Jiang D (2011). **Distinct cytoskeleton populations and extensive crosstalk**
593 **control *Ciona* notochord tubulogenesis** *Development* **138**:1631-1641.
594 https://doi.org/10.1242/dev.057208
595
596 Espinoza-Fonseca L M, Colson B A, Thomas D D (2014). **Effects of pseudophosphorylation**
597 **mutants on the structural dynamics of smooth muscle myosin regulatory light chain**
598 *Molecular Biosystems* **10**:2693-2698. https://doi.org/10.1039/c4mb00364k
599
600 Even-Ram S, Doyle A D, Conti M A, Matsumoto K, Adelstein R S, Yamada K M (2007). **Myosin**
601 **IIA regulates cell motility and actomyosin-microtubule crosstalk** *Nature Cell Biology*
602 **9**:299-309. https://doi.org/10.1038/ncb1540
603
604 Fiuza U-M, Lemaire P (2021). **Mechanical and genetic control of ascidian endoderm**

605 **invagination during gastrulation** *Seminars in Cell and Developmental Biology*
606 **120**:108-118. https://doi.org/10.1016/j.semcdb.2021.08.001
607
608 Fristrom D (1988). **The cellular basis of epithelial morphogenesis. A review** *Tissue and Cell*
609 **20**:645-690. https://doi.org/10.1016/0040-8166(88)90015-8
610
611 Glantz S T, Berlew E E, Chow B Y (2019). **Synthetic cell-like membrane interfaces for probing**
612 **dynamic protein-lipid interactions** *Methods in Enzymology* **622**:249-270.
613 https://doi.org/10.1016/bs.mie.2019.02.015
614
615 Glantz S T, Berlew E E, Jaber Z, Schuster B S, Gardner K H, Chow B Y (2018). **Directly**
616 **light-regulated binding of RGS-LOV photoreceptors to anionic membrane**
617 **phospholipids** *Proceedings of the National Academy of Sciences of the United States*
618 *of America* **115**:E7720-e7727. https://doi.org/10.1073/pnas.1802832115
619
620 Hashimoto H, Munro E (2019). **Differential expression of a classic cadherin directs tissue-level**
621 **contractile asymmetry during neural tube closure** *Developmental Cell*
622 **51**:158-172.e154. https://doi.org/10.1016/j.devcel.2019.10.001
623
624 Hashimoto H, Robin F B, Sherrard K M, Munro E M (2015). **Sequential contraction and**
625 **exchange of apical junctions drives zippering and neural tube closure in a simple**
626 **chordate** *Developmental Cell* **32**:241-255.

https://doi.org/10.1016/j.devcel.2014.12.017

Hotta K, Dauga D, Manni L (2020). **The ontology of the anatomy and development of the solitary ascidian *Ciona*: the swimming larva and its metamorphosis** *Scientific Reports* **10**:17916. https://doi.org/10.1038/s41598-020-73544-9

Hotta K, Mitsuhara K, Takahashi H, Inaba K, Oka K, Gojobori T, Ikeo K (2007). **A web-based interactive developmental table for the ascidian *Ciona intestinalis*, including 3D real-image embryo reconstructions: I. From fertilized egg to hatching larva** *Developmental Dynamics* **236**:1790-1805. https://doi.org/10.1002/dvdy.21188

Iwasaki T, Murata-Hori M, Ishitobi S, Hosoya H (2001). **Diphosphorylated MRLC is required for organization of stress fibers in interphase cells and the contractile ring in dividing cells** *Cell Structure and Function* **26**:677-683. https://doi.org/10.1247/csf.26.677

Jin P, Jan L Y, Jan Y N (2020). **Mechanosensitive ion channels: structural features relevant to mechanotransduction mechanisms** *Annual Review of Neuroscience* **43**:207-229. https://doi.org/10.1146/annurev-neuro-070918-050509

Kiehart D P (2015). **Epithelial morphogenesis: apoptotic forces drive cell shape changes** *Developmental Cell* **32**:532-533. https://doi.org/10.1016/j.devcel.2015.02.020

649 Kondo T, Hayashi S (2013). **Mitotic cell rounding accelerates epithelial invagination** *Nature*
650 **494**:125-129. https://doi.org/10.1038/nature11792
651
652 Kourakis M J, Newman-Smith E, Smith W C (2010). **Key steps in the morphogenesis of a**
653 **cranial placode in an invertebrate chordate, the tunicate *Ciona savignyi***
654 *Developmental Biology* **340**:134-144. https://doi.org/10.1016/j.ydbio.2010.01.016
655
656 Lecuit T, Lenne P F, Munro E (2011). **Force generation, transmission, and integration during**
657 **cell and tissue morphogenesis** *Annual Review of Cell and Developmental Biology*
658 **27**:157-184. https://doi.org/10.1146/annurev-cellbio-100109-104027
659
660 Lee J Y, Harland R M (2007). **Actomyosin contractility and microtubules drive apical**
661 **constriction in *Xenopus* bottle cells** *Developmental Biology* **311**:40-52.
662 https://doi.org/10.1016/j.ydbio.2007.08.010
663
664 Lu Q, Gao Y, Fu Y, Peng H, Shi W, Li B, Lv Z, Feng X Q, Dong B (2020). ***Ciona* embryonic tail**
665 **bending is driven by asymmetrical notochord contractility and coordinated by epithelial**
666 **proliferation** *Development* **147**:dev185868. https://doi.org/10.1242/dev.185868
667
668 Manjón C, Sánchez-Herrero E, Suzanne M (2007). **Sharp boundaries of Dpp signalling trigger**
669 **local cell death required for *Drosophila* leg morphogenesis** *Nature Cell Biology*
670 **9**:57-63. https://doi.org/10.1038/ncb1518

671

672 Martin K, Reimann A, Fritz R D, Ryu H, Jeon N L, Pertz O (2016). **Spatio-temporal**
673 **co-ordination of RhoA, Rac1 and Cdc42 activation during prototypical edge protrusion**
674 **and retraction dynamics** *Scientific Reports* **6**:21901. https://doi.org/10.1038/srep21901

675

676

677 Matter K, Balda M S (2003). **Functional analysis of tight junctions** *Methods* **30**:228-234.
678 https://doi.org/10.1016/s1046-2023(03)00029-x

679

680 Monier B, Gettings M, Gay G, Mangeat T, Schott S, Guarner A, Suzanne M (2015).
681 **Apico-basal forces exerted by apoptotic cells drive epithelium folding** *Nature*
682 **518**:245-248. https://doi.org/10.1038/nature14152

683

684 Nagafuchi A (2001). **Molecular architecture of adherens junctions** *Current Opinion in Cell*
685 *Biology* **13**:600-603. https://doi.org/10.1016/s0955-0674(00)00257-x

686

687 Nishimura M, Inoue Y, Hayashi S (2007). **A wave of EGFR signaling determines cell alignment**
688 **and intercalation in the *Drosophila* tracheal placode** *Development* **134**:4273-4282.
689 https://doi.org/10.1242/dev.010397

690

691 Osswald M, Barros-Carvalho A, Carmo A M, Loyer N, Gracio P C, Sunkel C E, Homem C C F,
692 Januschke J, Morais-de-Sá E (2022). **aPKC regulates apical constriction to prevent**

693 **tissue rupture in the *Drosophila* follicular epithelium** *Current Biology*
694 **32**:4411-4427.e4418. https://doi.org/10.1016/j.cub.2022.08.063
695
696 Pearl E J, Li J, Green J B (2017). **Cellular systems for epithelial invagination** *Philosophical*
697 *Transactions of the Royal Society of London. Series B, Biological Sciences*
698 **372**:20150526. https://doi.org/10.1098/rstb.2015.0526
699
700 Peng H, Qiao R, Dong B (2020). **Polarity establishment and maintenance in ascidian**
701 **notochord** *Frontiers in Cell and Developmental Biology* **8**:597446.
702 https://doi.org/10.3389/fcell.2020.597446
703
704 Popkova A, Andrenšek U, Pagnotta S, Ziherl P, Krajnc M, Rauzi M (2024). **A mechanical wave**
705 **travels along a genetic guide to drive the formation of an epithelial furrow during**
706 ***Drosophila* gastrulation** *Developmental Cell* **59**:400-414.e405.
707 https://doi.org/10.1016/j.devcel.2023.12.016
708
709 Qiao J, Peng H, Dong B (2023). **Development and application of an optogenetic manipulation**
710 **system to suppress actomyosin activity in *Ciona* epidermis** *International Journal of*
711 *Molecular Sciences* **24**:5707. https://doi.org/10.3390/ijms24065707
712
713 Schottenfeld J, Song Y, Ghabrial A S (2010). **Tube continued: morphogenesis of the**
714 ***Drosophila* tracheal system** *Current Opinion in Cell Biology* **22**:633-639.

https://doi.org/10.1016/j.ceb.2010.07.016

Sherrard K, Robin F, Lemaire P, Munro E (2010). **Sequential activation of apical and basolateral contractility drives ascidian endoderm invagination** *Current Biology* **20**:1499-1510. https://doi.org/10.1016/j.cub.2010.06.075

Shi W, Duclut C, Xu Y, Ma Y, Qiao J, Lin B, Yang D, Prost J, Dong B (2025). **Physics of notochord tube expansion in ascidians** *Proceedings of the National Academy of Sciences of the United States of America* **122**:e2419960122. https://doi.org/10.1073/pnas.2419960122

Štorgel N, Krajnc M, Mrak P, Štrus J, Ziherl P (2016). **Quantitative morphology of epithelial folds** *Biophysical Journal* **110**:269-277. https://doi.org/10.1016/j.bpj.2015.11.024

Sui L, Alt S, Weigert M, Dye N, Eaton S, Jug F, Myers E W, Jülicher F, Salbreux G, Dahmann C (2018). **Differential lateral and basal tension drive folding of *Drosophila* wing discs through two distinct mechanisms** *Nature Communications* **9**:4620. https://doi.org/10.1038/s41467-018-06497-3

Tepass U (2002). **Adherens junctions: new insight into assembly, modulation and function** *Bioessays* **24**:690-695. https://doi.org/10.1002/bies.10129

737 Vicente-Manzanares M, Ma X, Adelstein R S, Horwitz A R (2009). **Non-muscle myosin II takes**
738 **centre stage in cell adhesion and migration** *Nature Reviews Molecular Cell Biology*
739 **10**:778-790. https://doi.org/10.1038/nrm2786
740
741 Yamamoto K, Miura H, Ishida M, Mii Y, Kinoshita N, Takada S, Ueno N, Sawai S, Kondo Y,
742 Aoki K (2021). **Optogenetic relaxation of actomyosin contractility uncovers**
743 **mechanistic roles of cortical tension during cytokinesis** *Nature Communications*
744 **12**:7145. https://doi.org/10.1038/s41467-021-27458-3
745
746 Zartman J J, Shvartsman S Y (2010). **Unit operations of tissue development: epithelial folding**
747 *Annual Review of Chemical and Biomolecular Engineering* **1**:231-246.
748 https://doi.org/10.1146/annurev-chembioeng-073009-100919
749
750 Zhao L, Gao F, Gao S, Liang Y, Long H, Lv Z, Su Y, Ye N, Zhang L, Zhao C, Wang X, Song W,
751 Zhang S, Dong B (2021). **Biodiversity-based development and evolution: the**
752 **emerging research systems in model and non-model organisms** *Science China. Life*
753 *Sciences* **64**:1236-1280. https://doi.org/10.1007/s11427-020-1915-y
754
755
756

Figure legends

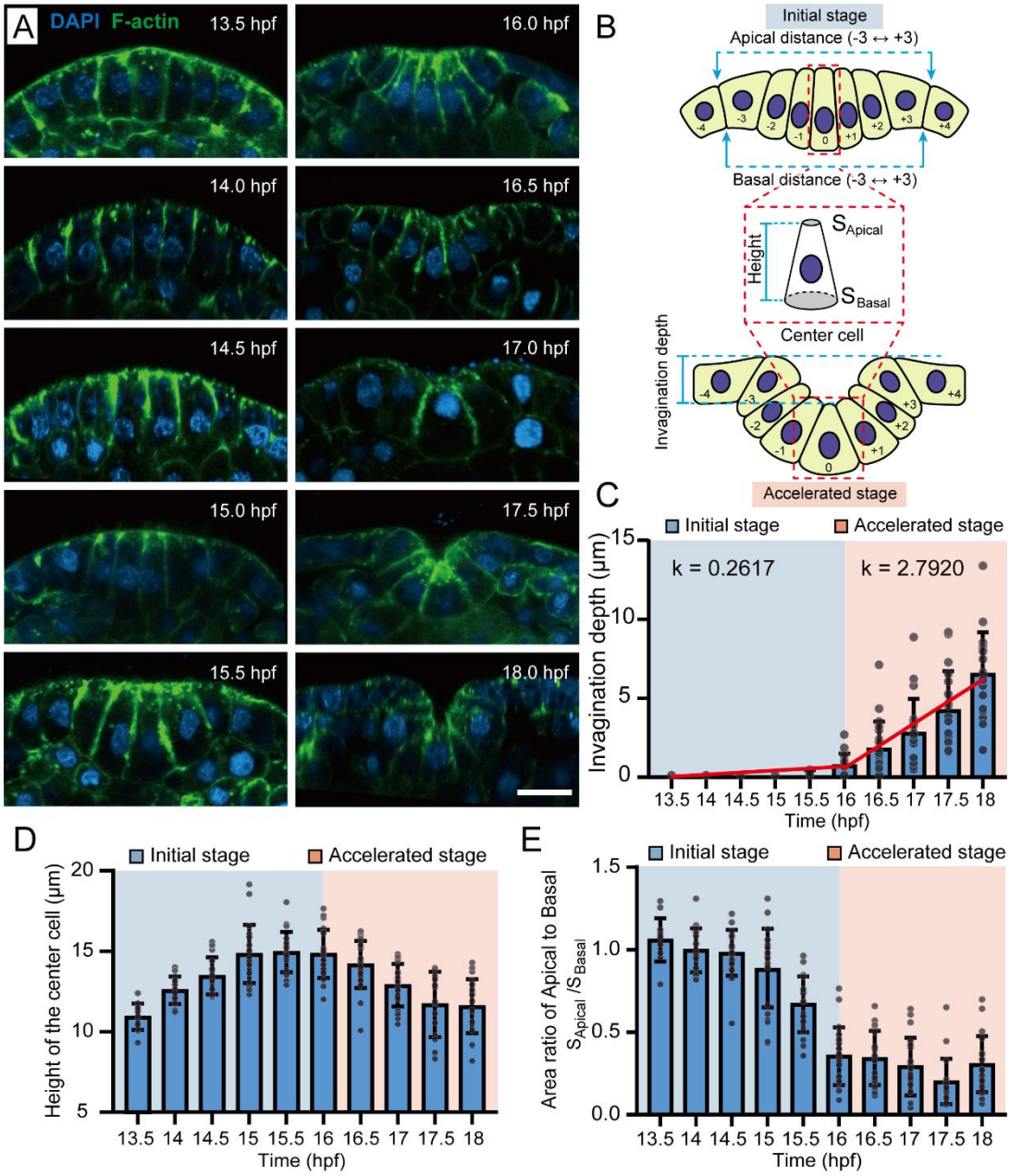

Figure 1. Cellular processes of *Ciona* atrial siphon tube invagination.

(A) Representative images of atrial siphon morphogenesis in *Ciona* embryos from 13.5 hpf to 18 hpf. Scale bar: 10 μm.

(B) Measurement parameters of the *Ciona* atrial siphon. The cell undergoing the most prominent apical constriction at the center of invagination was defined as the center cell (0). The adjacent cells on the left and right were defined sequentially as -1, -2, -3, -4 and +1, +2, +3, +4, respectively.

(C) Quantification of the invagination depth in the atrial siphon of *Ciona*

embryos. Red lines indicate linear regression fits of invagination depth during the initial (13.5-16 hpf, k = 0.2617) and accelerated (16-18 hpf, k = 2.7920) stages. n = 20.

(D, E) Quantification of the center cell height and apical-to-basal area ratio at the atrial siphon of *Ciona* embryos. The blue-shaded region represents the initial stage, while the orange-shaded region indicates the accelerated stage. n = 20.

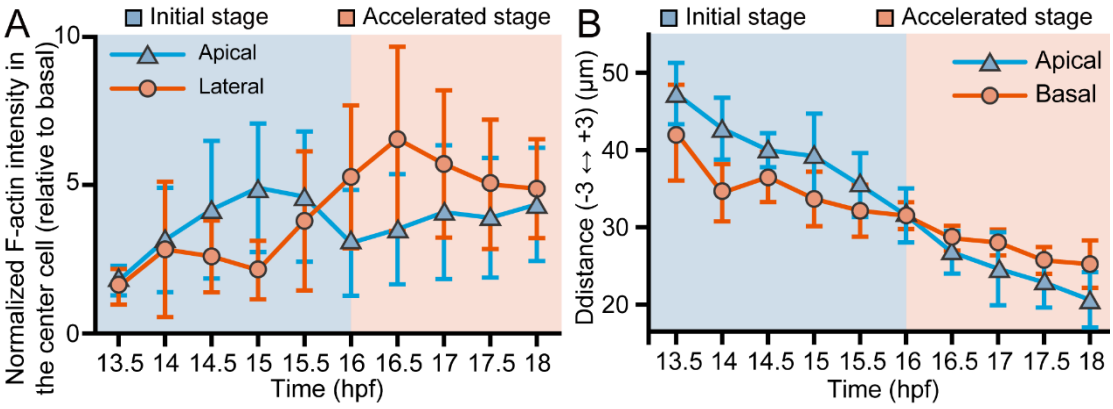

Figure 1—figure supplement 1. Quantification of F-actin intensity and intercellular distance during *Ciona* atrial siphon morphogenesis.

(A) Normalized F-actin intensity at the apical and lateral regions of center cells during *Ciona* atrial siphon morphogenesis (basal level set to 1).

(B) Quantification of the linear distance between the -3/-4 and +3/+4 cell junctions at the apical or basal surface in the atrial siphon of *Ciona* embryos. The blue-shaded region represents the initial stage, while the orange-shaded region indicates the accelerated stage. Representative images are shown in Figure 1A. n = 20.

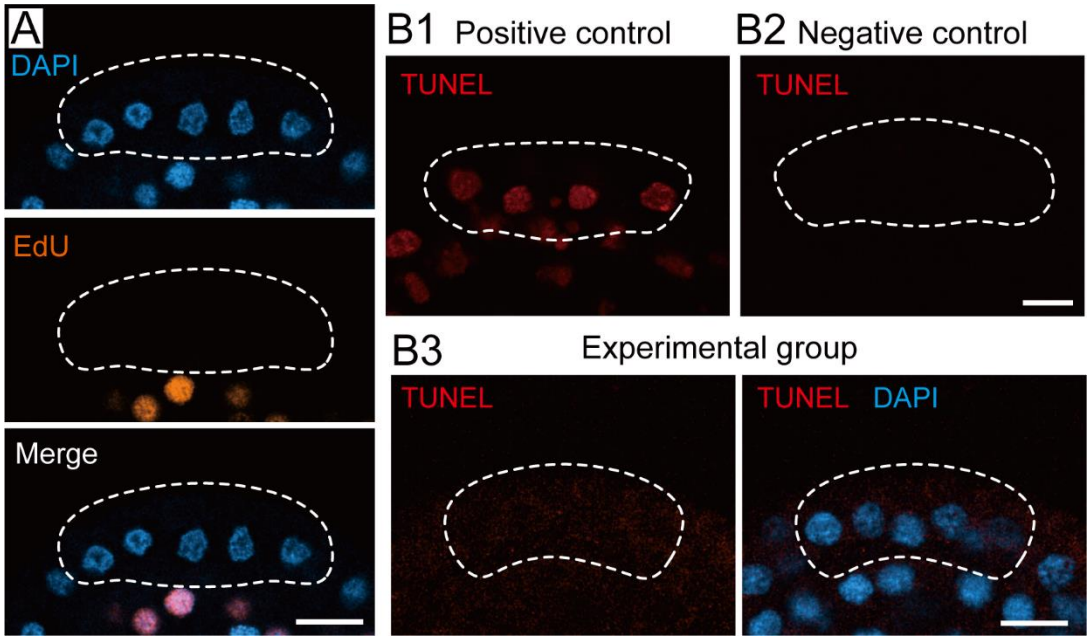

Figure 1—figure supplement 2. EdU and TUNEL staining during *Ciona* atrial siphon morphogenesis.

(A) Representative images of EdU staining at 14-15 hpf. Orange: EdU-positive nuclei indicating cell proliferation. Blue: DAPI. No EdU signal was detected in the atrial siphon primordium (white dashed outline). Scale bar: 10 μm. n = 10. (B1-3) Representative images of TUNEL staining at 15 hpf. (B1) Positive control: DNase I pretreatment (20 U/mL, 10 min) induced DNA fragmentation. (B2) Negative control: staining performed without terminal deoxynucleotidyl transferase (TdT) enzyme. (B3) Experimental group: no detectable TUNEL signal in the atrial siphon primordium (white dashed outline). Scale bar: 10 μm. n = 10.

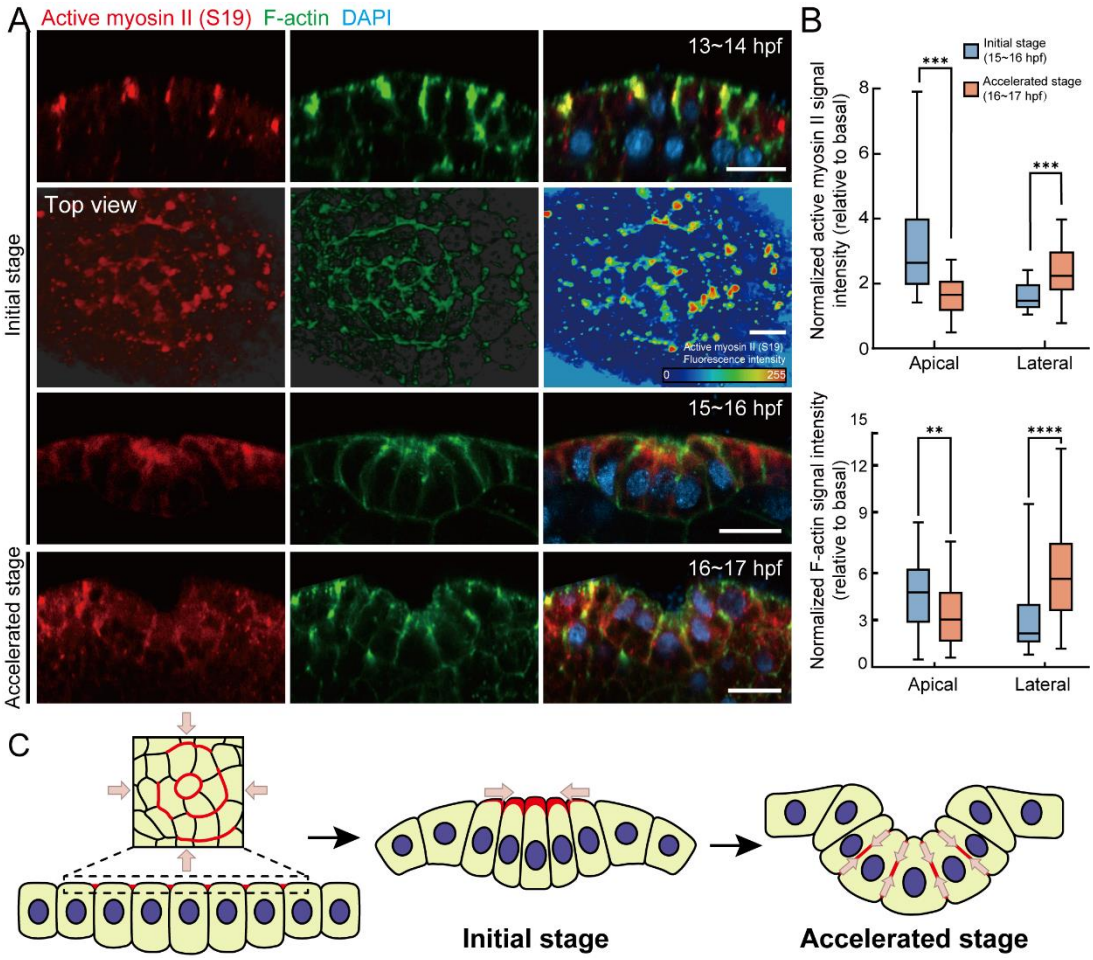

Figure 2. Bidirectional translocation of actomyosin between apical and lateral domains during atrial siphon tube invagination.

(A) Representative images of *Ciona* embryos stained for active myosin II (anti-pS19 MRLC，red) and F-actin (green) at different stages of atrial siphon invagination. The heatmap color scale represents the fluorescence intensity of myosin II signal (8-bit grayscale range: 0-255), with red indicating the highest intensity. Scale bar: 10 μm.

(B) Normalized fluorescence intensity of active myosin II (anti-pS19 MRLC) and F-actin at the apical and lateral regions of center cells during different stages of atrial siphon invagination (basal level set to 1). **$p < 0.01$, ***$p < 0.001$, ****$p < 0.0001$, $n = 20$.

(C) Schematic model illustrating the mechanical forces driving atrial siphon primordium invagination. Brown arrows indicate the direction of contractile forces; red areas depict active myosin II localization.

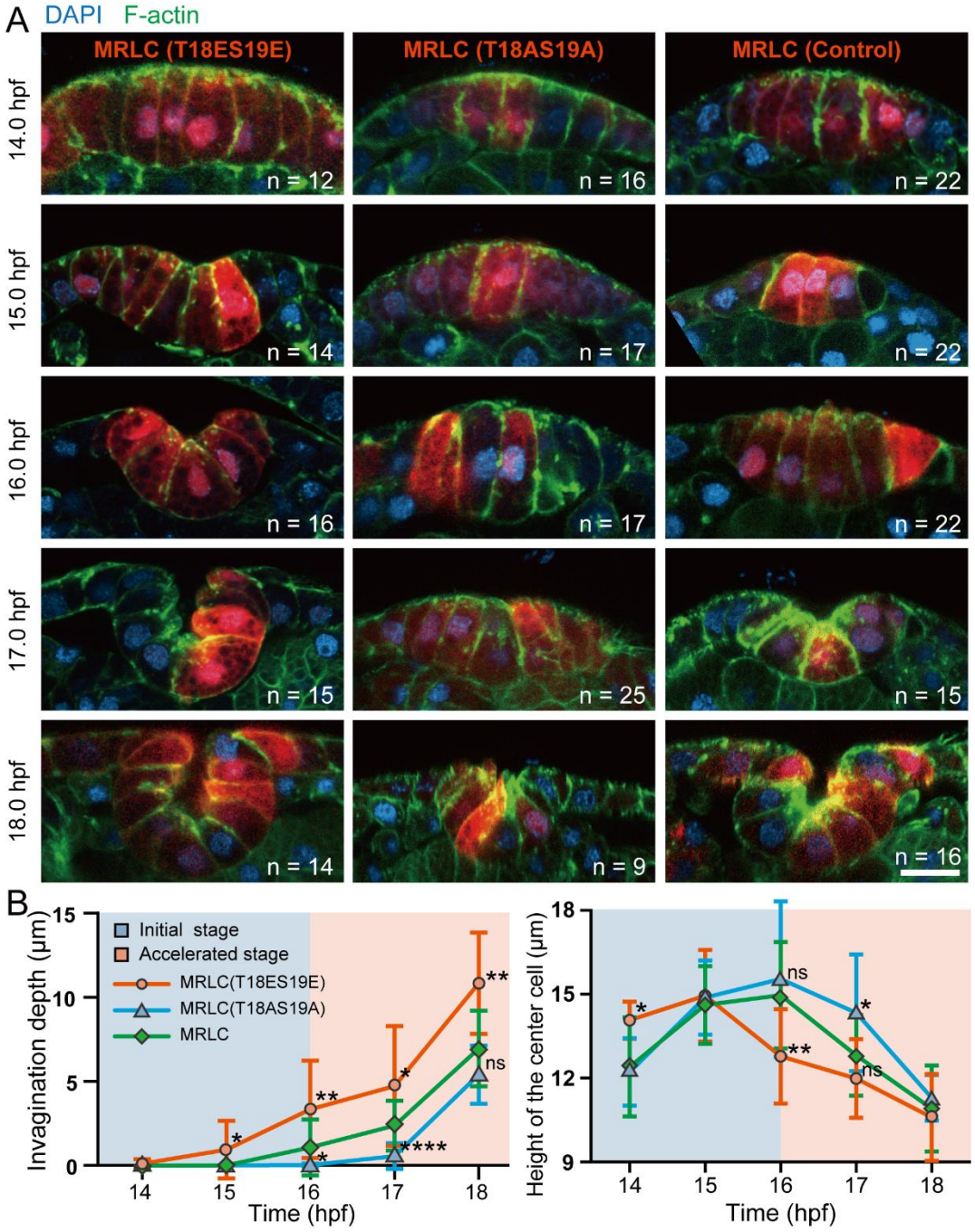

Figure 3. Modulation of atrial siphon invagination by overexpression of myosin mutants

(A) Representative images of *Ciona* atrial siphon primordium expressing wild-type and mutant MRLC constructs. Scale bar: 10 μm.

(B) Quantification of invagination depth and the center cell height in MRLC (T18ES19E), MRLC (T18AS19A), and MRLC groups. The blue-shaded region represents the initial stage, while the orange-shaded region indicates the accelerated stage. *p < 0.05, **p < 0.01, ***p < 0.001, ****p < 0.0001.

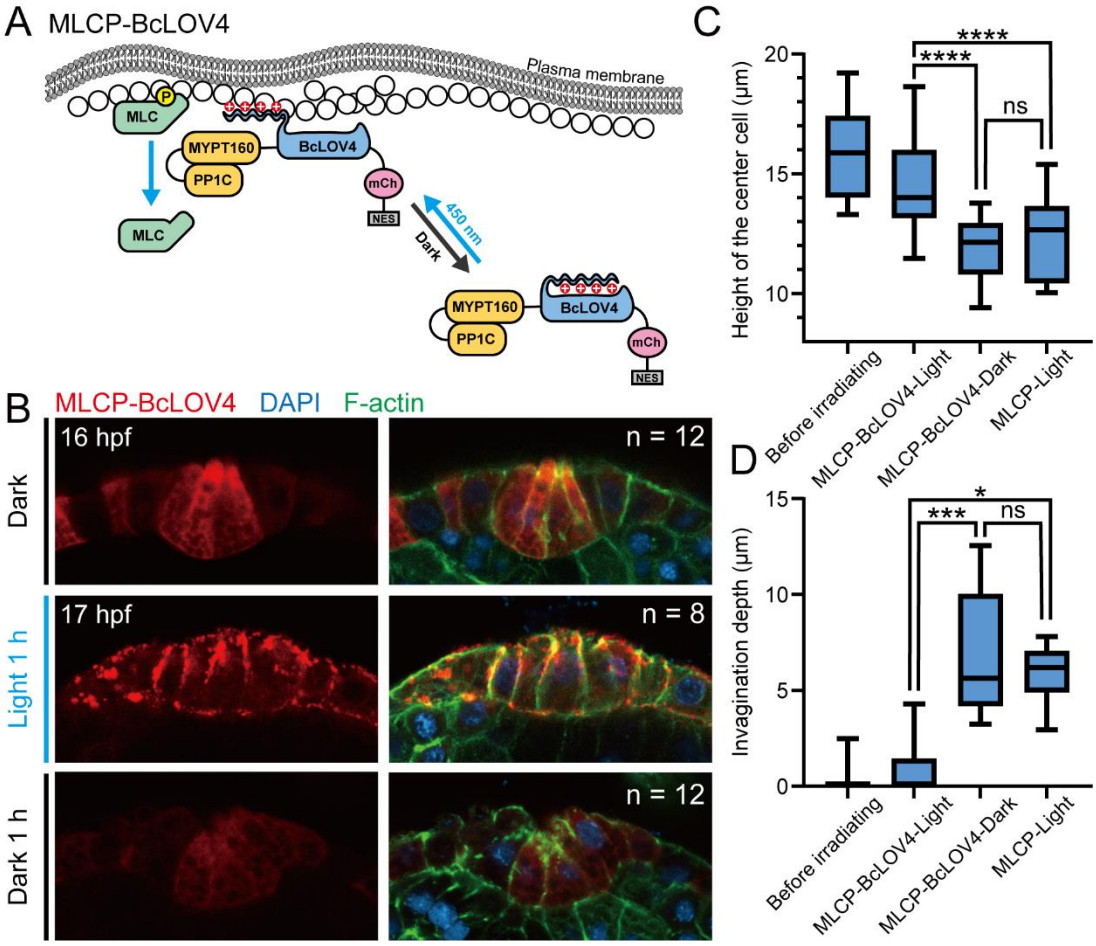

Figure 4. Disruption of contractile forces during rapid invagination of the *Ciona* atrial siphon using an optogenetic system

(A) Schematic diagram depicting the structure and mechanism of the MLCP-BcLOV4 system. The PP1C::MYPT169::BcLOV4::mCherry::NES fusion protein is initially dispersed in the cytoplasm. Upon exposure to blue light, BcLOV4 undergoes a conformational change, allowing it to interact electrostatically with the plasma membrane. This leads to the recruitment of the PP1C and MYPT169 components, subunits of myosin light chain phosphatase (MLCP), to the membrane, where they reduce myosin activity.

(B) Representative images of developmental progression in the MLCP-BcLOV4 expression group exposed to blue light for 1 h, and in the dark control group maintained in darkness for 1 h. Scale bar: 10 μm.

(C, D) Quantification of invagination depth and the center cell height in the MLCP-BcLOV4 expression group, the dark control group and MLCP control group (Figure 4—figure supplement 1). *$p < 0.05$, ***$p < 0.001$, ****$p < 0.0001$.

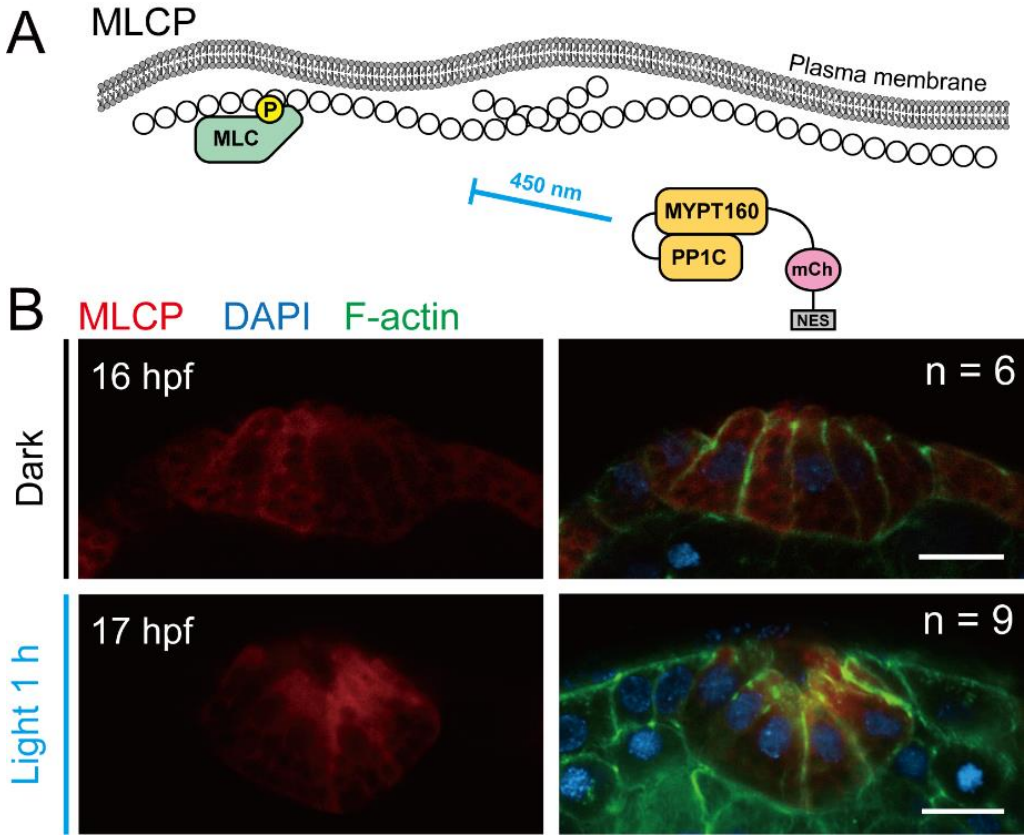

Figure 4—figure supplement 1. MRCL control group in the optogenetic experiment

(A) Schematic diagram depicting the structure and mechanism of the MLCP control system. The PP1C::MYPT169::mCherry::NES fusion protein remained diffuse in the cytoplasm under light exposure and failed to function.

(B) Representative images of developmental progression in the MLCP control group exposed to blue light for 1 h. Scale bar: 10 μm.

Figure 4—video 1. The developmental processes of the MLCP control group under blue light illumination for 1 h. Scale bar: 10 μm.

Figure 4—video 2. The developmental processes of MLCP-BcLOV4-expressed group under blue light illumination for 1 h. Scale bar: 10 μm.

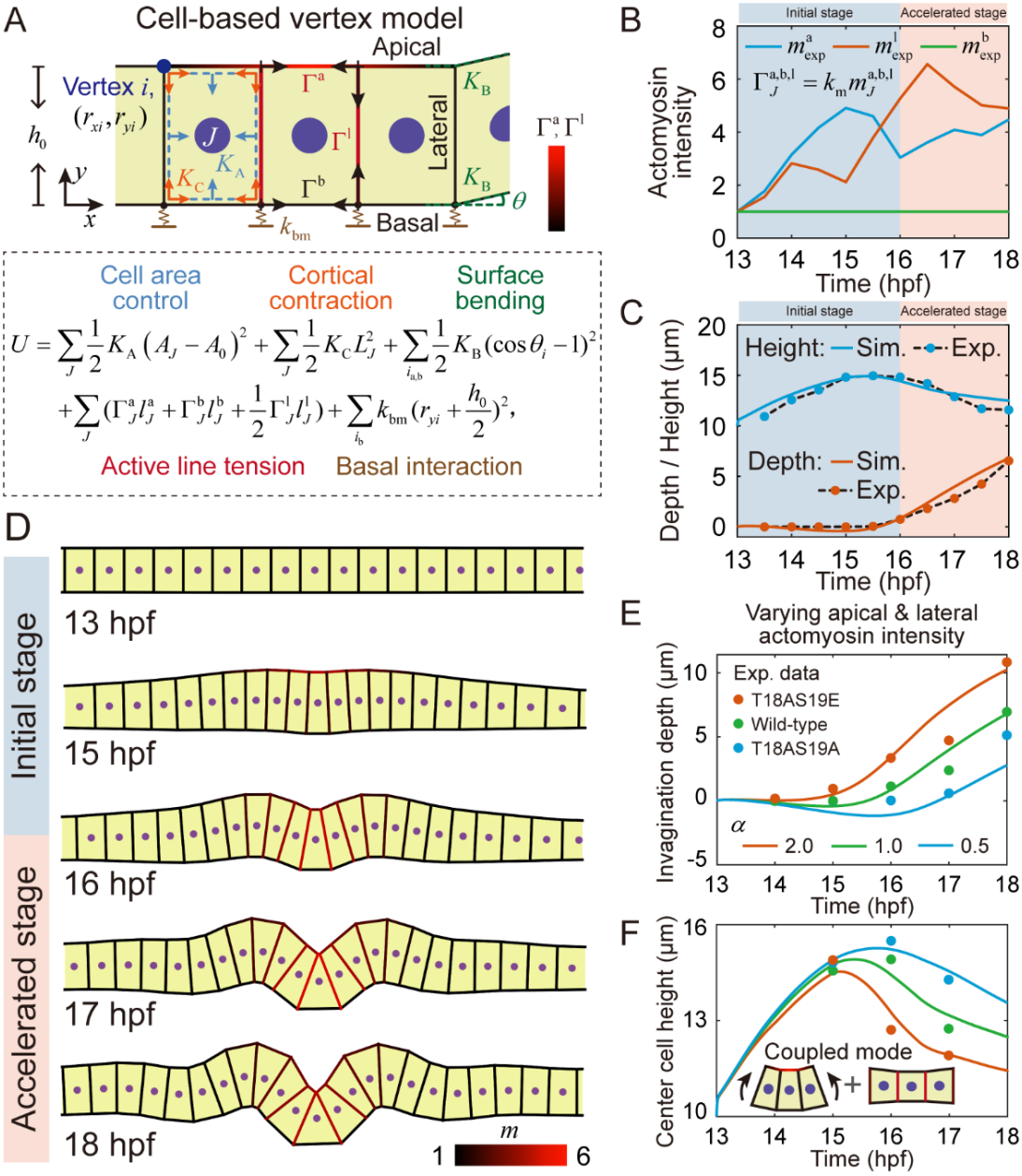

Figure 5. Simulations and analysis based on vertex model

(A) Schematic of the cell-based vertex model. The epithelial tissue is constructed by the apical, basal, and lateral vertices and edges. The effective energy U takes into cell area constraint (modulus K_A), passive cortical contraction (coefficient K_C), tissue surface bending (modulus K_B), basal interaction (coefficient k_{bm}), and apical, basal and lateral active tensions (Γ^a, Γ^l and Γ^b, respectively). $\mathbf{r}_i = (r_{xi}, r_{yi})$ denotes the Cartesian coordinates of vertex i. A_J, L_J, and $l_J^{a,b,l}$ are the area, perimeter, and length of apical, basal,

lateral edges of cell J. θ_i represents the angle between adjacent apical or basal edges connected to vertex i. A_0 is the reference area and h_0 is the initial cell height.

(B) Temporal evolution of actomyosin intensities at the apical, lateral, and basal domains of the center cell in the model, parameterized based on experimentally measured F-actin distribution. The blue-shaded and orange-shaded regions represent the apical constriction stage, and the invagination stage, respectively.

(C) Evolution curves of invagination depth (blue) and center cell height (orange) in simulations. Dots represent corresponding experimentally measured values.

(D) Snapshots at specific timepoints during simulation progression. The colors of edges represent actomyosin intensity.

(E, F) Invagination depth (E) and center cell height (F) regulated by changes in actomyosin intensities under the scaling factor α at both apical and lateral regions of all cells. The data points are from the mutant experiments in Figure 3B.

Figure 5—video 1. Vertex model simulation.

Top row: Progression of the vertex model simulation. Edge colors represent actomyosin intensity.

Bottom row (left to right):

1. Evolution curves of invagination depth;
2. Evolution curves of center cell height;
3. Temporal evolution of actomyosin intensities at the apical, lateral, and basal domains of the center cell in the model, parameterized based on experimentally measured F-actin distribution.

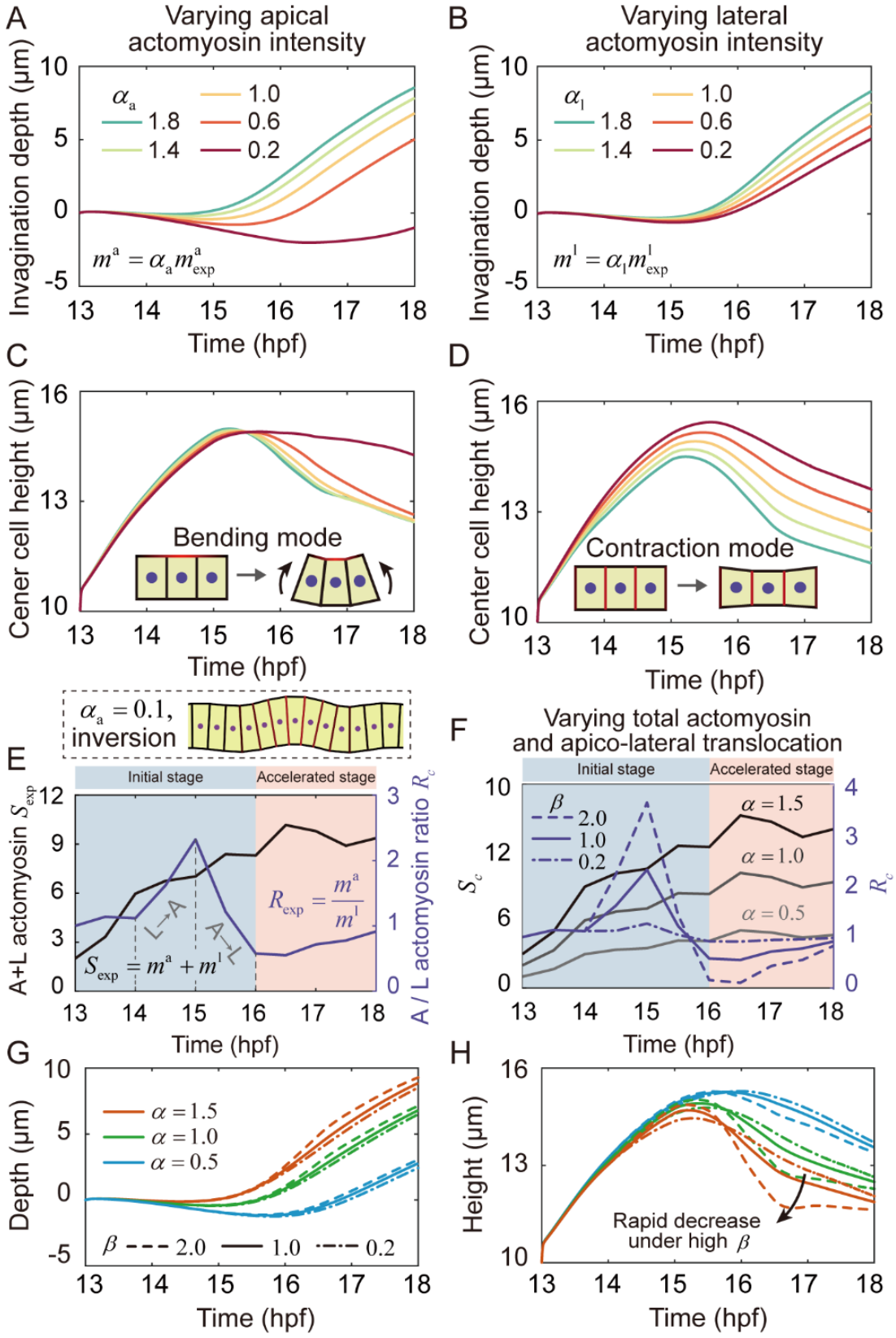

905

906

907

908

909

Figure 6. Mechanics of epithelial invagination revealed by vertex model simulations

(A, C) Invagination depth (A) and center cell height (C) under varying apical actomyosin intensity represented by a scaling factor α_{a}, with the lateral intensity unchanged. A Schematic illustration of the bending mode induced by apicobasal imbalance is presented. A snapshot of a specific inversed evagination modeling under $\alpha_{\mathrm{a}} = 0.1$ is shown.

(B, D) Invagination depth (B) and center cell height (D) under varying lateral actomyosin intensity represented by a scaling factor α_{l}, with the apical intensity unchanged. A Schematic illustration of the contraction mode induced by lateral tension is presented.

(E) Temporal evolution of the sum S_{exp} and ratio R_{exp} of apical and lateral actomyosin intensities in the center cell in experiments.

(F) Varying sum S_c and ratio R_{c} of actomyosin intensities regulated by α and β in simulations.

(G, H) Invagination depth (G) and center cell height (H) under varying α and β.

Appendix 1—table 1. Key resource table

REAGENT or RESOURCE	SOURCE	IDENTIFIER
antibodies		
Phospho-Myosin Light Chain 2 (Ser19) Antibody	Cell Signaling	#3671
Alexa Fluor 647 anti-Mouse IgG	Invitrogen	#A28181
Chemicals		
EdU Cell Proliferation Kit with AF555	BeyoClick	C0075S
Alexa Fluor™ 488 Phalloidin	Thermo fisher	A12379
Protease E	sigma-Aldrich	P5147
Sodium thioglycolate	sigma-Aldrich	T0632
D-mannitol	sigma-Aldrich	M4125
MS-222	sigma-Aldrich	E10521
VECTASHIELD® with DAPI	Vectorlabs	H1200
Phanta Max Super-Fidelity DNA Polymerase	Vazyme	P505
ClonExpress MultiS One Step Cloning Kit	Vazyme	C113
TUNEL BrightRed Apoptosis Detection Kit	Vazyme	A113
Plasmids		
Epi1> MRLC::mCherry	This study	N/A
Epi1> MRLC(T18AS19A)::mCherry		N/A
Epi1> MRLC(T18ES19E)::mCherry		N/A
Epi1>PP1c::MYPT169::BcLOV4::mCherry::NES		N/A
Epi1>PP1c::MYPT169::mCherry::NES		N/A
Software		
ImageJ	NIH Image	https://imagej.nih.gov/ij/
Prism 10 CN	Graphpad Software	https://www.graphpad.com/
Imaris 10	Oxford Instruments	https://imaris.oxinst.com/
MATLAB R2021a	MathWorks	https://www.mathworks.com/

Appendix 1—table 2. Primer sequences used in this study

Construct name	Primers	Sequence (5'→3')
MRLC	Forward	ATGTCG-AGCCGACGAACTAAA
	Reverse	CTAAATGTCATCTTTTTCTTTAGCG
MRLC(T18AS19A)	Forward	TGCAGCCGCCAATGTCTTTGCTATGTTCGATCAAGC
	Reverse	GACATTGGCGGCTGCACGCTGGGCGCGC
MRLC(T18ES19E)	Forward	TGCAGAAGAAAATGTCTTTGCTATGTTCGATCAAGCT
	Reverse	AGACATTTTCTTCTGCACGCTGGGCGCG
BcLOV4	Forward	ATGGCCACAGACGCAATCG
	Reverse	GATTATGATCTAGAGTC
PP1c	Forward	ATGGCGGACGGGGAGC
	Reverse	CCTTTTCTTCGGCGGA
MYPT169	Forward	ATGAAGATGGCGGACGCG
	Reverse	AGCTGCTTCTATATCAACCCCTTG